

Probing Nonadiabatic Dynamics with Attosecond Pulse Trains and Soft X-ray Raman Spectroscopy

Lorenzo Restaino, Deependra Jadoun, and Markus Kowalewski*

Department of Physics, Stockholm University, Albanova University Centre, SE-106 91 Stockholm, Sweden

Linear off-resonant X-ray Raman techniques are capable of detecting the ultrafast electronic coherences generated when a photoexcited wave packet passes through a conical intersection. A hybrid femtosecond or attosecond probe pulse is employed to excite the system and stimulate the emission of the signal photon, where both fields are components of a hybrid pulse scheme. In this paper, we investigate how attosecond pulse trains, as provided by high-harmonic generation processes, perform as probe pulses in the framework of this spectroscopic technique, instead of single Gaussian pulses. We explore different combination schemes for the probe pulse, as well as the impact of parameters of the pulse trains on the signals. Furthermore, we show how Raman selection rules and symmetry consideration affect the spectroscopic signal, and we discuss the importance of vibrational contributions to the overall signal. We use two different model systems, representing molecules of different symmetry, and quantum dynamics simulations to study the difference in the spectra. The results suggest that such pulse trains are well suited to capture the key features associated with the electronic coherence.

I. INTRODUCTION

Conical Intersections [1–4] (CIs) represent fast, radiationless decay channels in electronically excited molecules (see fig. 1(a)). Virtually present in every molecular system, CIs play a key role in charge transfer processes [5], reaction mechanisms [6] and in the vast majority of photochemical, photophysical and photobiological reactions [7–12], such as the *cis/trans* isomerization of retinal [13, 14]. At such intersections the Born-Oppenheimer approximation breaks down causing complex dynamics of the coupled vibronic states, which can be observed spectroscopically [15–17]. As the photoexcited wave packet comes closer to the conical intersection, the energy separation between the potential energy surfaces (PESs) rapidly decreases. Thus, detection requires an unusual combination of temporal and spectral resolution that is not available via conventional femtosecond optical and infrared (IR) experiments [14, 19–21]. However, pulses in the extreme ultraviolet (XUV) to the short X-ray spectral region possess the required combination to directly detect the passage through a CI [22–30]. Single attosecond pulses (SAPs) have been extensively used in pump-probe experiments. Although the availability of such pulses has seen a significant increase thanks to high-harmonic generation (HHG) [31, 32] and free electron lasers (FELs) [33] sources, the generation of SAPs still requires a complex setup. The HHG process in gases emits a sequence of short bursts of radiation, which are coherently driven by the generation laser, where emission events occur during each laser half cycle. Each of these short bursts is in the attosecond regime and their interference leads to the observation of odd harmonics. Such attosecond pulse trains (APT) [34, 35], unlike isolated pulses [36, 37], are directly available in a HHG setup, which is a table-

top source now widely found in many laboratories. Recent theoretical developments have showed the capability of APTs to probe the electronic coherence created by the CI in the context of time-resolved photoelectron spectroscopy [38] and time-resolved electron-momentum imaging [39].

In this paper, we demonstrate theoretically how APTs perform as probes in the framework of the transient redistribution of ultrafast electronic coherences in attosecond Raman signals (TRUECARS) technique [40] to probe electronic coherences generated by a wave packet passing through a CI. We use two different model systems that represent molecules of different symmetry and use quantum dynamics simulations to study the difference in the spectrum.

II. SPECTROSCOPIC SIGNALS AND MODELS

A. The TRUECARS signal

The TRUECARS technique uses an off-resonant stimulated X-ray Raman process (see fig. 1(b) and (c)) which is sensitive to coherences rather than populations. In the X-ray Raman scheme, core-hole states are involved as intermediates rather than common valence excited states. As shown in fig. 1(b), the two pulses making up the hybrid pulse scheme, namely ε_1 and ε_0 , drive the Raman process, which is in turn detected by a heterodyne detection scheme, where a local oscillator is used. The frequency and time resolved signal reads in atomic units as follows:

$$S(\omega_R, T) = 2\Im \left\{ \int dt e^{i\omega_R(t-T)} \varepsilon_0^*(\omega_R) \times \varepsilon_1(t-T) \langle \hat{a}(t) \rangle \right\} \quad (1)$$

* e-mail: markus.kowalewski@fysik.su.se

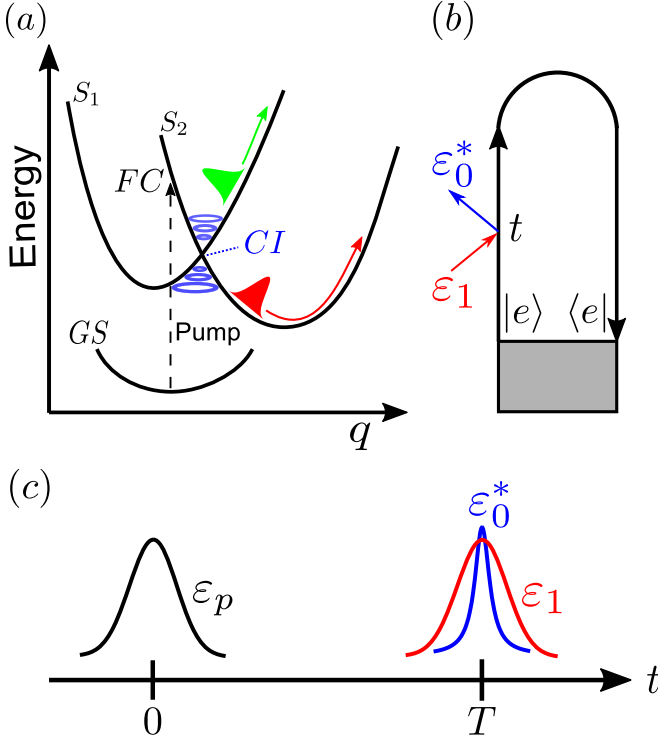


Figure 1. (a) Scheme of a CI: 1D cut of potential energy surfaces along a generic reaction coordinate, q . Following photoexcitation from the ground state (GS), the wave packet reaches the CI from the Frank-Condon (FC) region. (b) Loop diagram [18] of the off-resonant stimulated Raman signal. The grey area represents the preparation of the system into the excited state by means of a pump pulse, temporally well separated from the detection process. After photoexcitation, the system propagates freely for a delay time T before being probed by the hybrid-shaped pulse. (c) Schematics of the pump (ε_p) and hybrid probe pulse ($\varepsilon_1, \varepsilon_0^*$) setup in TRUE-CARS.

where T is the time delay between the probe field and the preparation pulse (see fig. 1(c)), $\langle \hat{a}(t) \rangle$ is the time dependent expectation value of the X-ray transition polarizability and ω_R is the Raman shift. For the details of the signal, see Ref. [40]. The dependence on the dynamics of the system enters the TRUE-CARS signal through $\langle \hat{a} \rangle$. Additional details on \hat{a} are given in subsection C.

The TRUE-CARS spectrum is characterized by an oscillating pattern of gain and loss features in the Stokes and anti-Stokes regime, that is only visible when a vibrational or electronic coherence is present. Assuming that both components of the probing field have the same carrier frequency, ω_X , the spectrum is going to be centered at a Raman shift of $\omega_R = 0$.

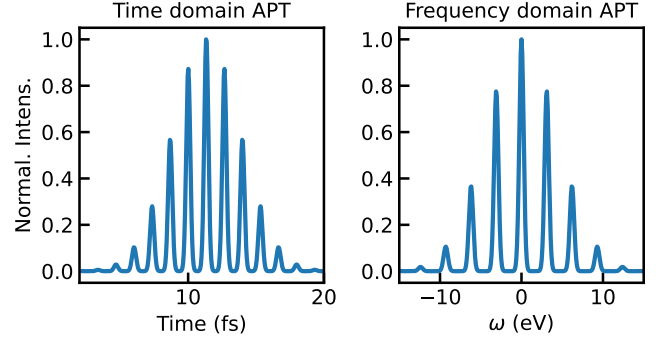


Figure 2. Snapshot of the modeled APT shape at $\omega_{IR} = 1.55$ eV. On the left: envelope of the pulse train in time domain. On the right: pulse train in frequency domain, shifted with respect to a selected central harmonic.

B. Modelling of the Pulse Trains

To illustrate how the pulse trains were built, we start from their definition in the time domain:

$$E_{APT}(t) = G(t)P(t) \quad (2)$$

where $G(t)$ is a Gaussian envelope of σ_{env} width

$$G(t) = e^{-t^2/2\sigma_{env}^2} \quad (3)$$

and $P(t)$ is an infinite train of pulses. The electric field of the single pulses inside the train is defined as

$$E_{SAP}(t) = e^{-\left(t - \frac{\tau}{2}\right)^2/2\sigma_{SAP}^2} \cos\left[\omega_X \left(t - \frac{\tau}{2}\right)\right] \quad (4)$$

with ω_X being the center frequency and $\tau = 2\pi/\omega_{IR}$ the period of the IR field. The expression for the electric field then reads:

$$E_{APT}(t) = e^{-t^2/2\sigma_{env}^2} \times \sum_n e^{-\left(t - n\frac{\tau}{2}\right)^2/2\sigma_{SAP}^2} \cos\left[\omega_X \left(t - n\frac{\tau}{2}\right) + n\pi\right]. \quad (5)$$

The pulse train employed in the calculations was built according to eq. (5) by substitution of t with $t - T$ and with the following parameters: $\sigma_{env} = 2.5$ fs and $\sigma_{SAP} = 0.15$ fs. For the purpose of simulating TRUE-CARS spectra, the center frequency ω_X can assume any arbitrary value.

To ease nomenclature, henceforth, single pulses in the femtosecond or attosecond regime will be broadly referred to as “Gaussian pulses”. A snapshot of the train pulse at $\omega_{IR} = 1.55$ eV is displayed in fig. 2. Snapshots at different frequencies of the IR laser are available in the SI.

C. Models and Symmetry

We use group theory to identify Raman active transitions and the vanishing integral rule to predict whether the polarizability matrix elements such as $\langle \Psi'' | \hat{\alpha} | \Psi' \rangle$ will be zero. In particular, they will vanish if the product of the irreducible representations of the two relevant states and the operator does not contain the totally symmetric representation, that is

$$\Gamma(\Psi'') \otimes \Gamma(\hat{\alpha}) \otimes \Gamma(\Psi') \not\supset \Gamma^{(s)}. \quad (6)$$

The two systems studied in this work belong to the C_i and to the C_s point groups, respectively. According to their character tables, the polarizability tensor elements α_{xx} , α_{yy} and α_{xy} all transform as the totally symmetric irreducible representation, i.e. A_g in C_i and A' in C_s . This was taken into account while modelling the X-ray polarizability operator, $\hat{\alpha}$, that was here approximated to a 2x2 matrix in the electronic subspace:

$$\hat{\alpha} = \begin{pmatrix} \alpha_{11} & \alpha_{12} \\ \alpha_{21} & \alpha_{22} \end{pmatrix}. \quad (7)$$

The full electronic polarizability matrix must be taken into account in order to be basis-independent (adiabatic vs. diabatic states) and the diagonal matrix elements cannot be neglected when transforming between representations. The diabatic wave function, $\Psi(\mathbf{q}, t)$, is expressed in terms of the electronic states. For a system with two electronic states, the wave function reads:

$$\Psi(\mathbf{q}, t) = \begin{pmatrix} \phi_1(\mathbf{q}, t) \\ \phi_2(\mathbf{q}, t) \end{pmatrix}. \quad (8)$$

Adiabatic and diabatic states are related by an unitary transformation, where the advantage of the diabatic basis is the absence of derivative couplings [41]. Expanding the expectation value, $\langle \hat{\alpha} \rangle$, yields:

$$\begin{aligned} \langle \hat{\alpha} \rangle &= \langle \Psi | \hat{\alpha} | \Psi \rangle \\ &= \langle \phi_1 | \alpha_{11} | \phi_1 \rangle + \langle \phi_2 | \alpha_{22} | \phi_2 \rangle + 2\Re \langle \phi_1 | \alpha_{12} | \phi_2 \rangle \end{aligned} \quad (9)$$

According to eq. (6), for a Raman active transition two conditions need to be fulfilled here: i) the diagonal and off-diagonal polarizability matrix elements must all transform as the totally symmetric irreducible representation of their point group (A_g in C_i and A' in C_s , respectively); ii) the electronic states ϕ_1 and ϕ_2 must have the same symmetry label, or else the integral $2\Re \langle \phi_1 | \alpha_{12} | \phi_2 \rangle$ will vanish. The diagonal, ($\langle \phi_1 | \alpha_{11} | \phi_1 \rangle + \langle \phi_2 | \alpha_{22} | \phi_2 \rangle$), and off-diagonal, ($2\Re \langle \phi_1 | \alpha_{12} | \phi_2 \rangle$), terms refer to vibrational and electronic contributions, respectively. Each vibrational normal mode has an associated irreducible representation, too. Therefore, the diagonal contribution will be suppressed if the vibrational modes transform as the wrong irreducible representation. In practice, we can ensure the transition will be Raman active if ϕ_1 , ϕ_2 and α_{ij} all fall into A_g for C_i and into A' for C_s .

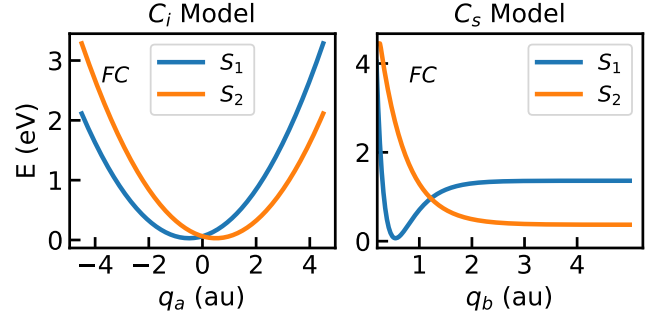


Figure 3. Potential energy surfaces of the investigated model systems. On the left: 1D cut of the diabatic potential energy surface along q_a , in the C_i system. On the right: 1D cut of the diabatic potential energy surface along q_b , in the C_s system. The wave packet has been previously excited from the ground state to the Franck-Condon (FC) region on S_2 by means of a pump pulse.

The concept of point groups is based on the approximation of a rigid molecule, that is considering the molecule as a rigid skeleton of nuclei. However, when large amplitude motions are considered where the symmetry of the system is not conserved, the concept is inadequate. Photoisomerization processes are well known examples of large amplitude nuclear motion in molecules. To generate symmetry adapted polarizability element functions in the diabatic basis, we now introduce the complete nuclear permutation inversion (CNPI) group [42]. A CNPI group consists of all permutations of identical nuclei, the inversion of all nuclear and electronic coordinates, (E^*), as well as their products. The inversion E^* differs from the inversion operation i in point groups. The former is an operation which results in a sign change of all nuclear and electronic coordinates in the space-fixed coordinate system. A similar application to electronic states and transition dipole moments can be found in Ref. [43]. Following these sections, details of the modeling of the two systems as well as the polarizability matrix are shown.

1. C_i Symmetry Model

This model consists of two harmonic potential wells shifted with respect to each other (see left panel of fig. 3). It represents two excited electronic states with a conical intersection. An example of such a molecule could be benzene (C_6H_6) and its photochemistry [44] or acetylene (C_2H_2) [45]. The diagonal and off-diagonal elements of the polarizability have been shaped by a function of q_1 and q_2 , which is symmetric with respect to the two normal modes. In the framework of CNPI this translates as

$$E^* \alpha_{ij}(q_1, q_2) = E^* \alpha_{ij}(-q_1, -q_2) = E^* \alpha_{ij}(q_1, q_2).$$

This function behaves non-linearly with respect to the nuclear coordinates in the proximity of the CI. In this

specific case, both normal modes q_1 and q_2 transform as the totally symmetric irreducible representation A_g , thus they are all Raman active. Plots of the symmetry adapted functions of the polarizability matrix elements as well as the single contributions to $\langle\hat{\alpha}\rangle$ are available in the SI.

2. C_s Symmetry Model

The C_s model consists of a Morse-like potential well and a repulsive potential with asymptotic behavior at large values of q , with a conical intersection. A 1D cut of the system is shown in the right panel of fig. 3. Hydroxylamine (NH_2OH), which has C_s symmetry, is a well-known example for the study of the effects of conical intersections in photodissociation [46]. Similarly to the C_i symmetry, the diagonal and off-diagonal elements of the polarizability have been here shaped by a function of q_1 and q_2 . This time, the function is symmetric with respect to q_2 and non-symmetric to q_1 . A fundamental transition is Raman active if a normal mode forms a basis for one or more components of the polarizability. Here, the normal mode q_1 transforms as the irreducible representation A'' , while q_2 as A' . Thus, q_2 is Raman active. Further details, including contour plots of the aforementioned functions, are available in the SI.

III. COMPUTATIONAL DETAILS

The time evolution was simulated by solving the time-dependent (non-relativistic) Schrödinger equation numerically with the Fourier method [47], where the wave function is represented on an equally spaced grid of sampling points in coordinate space, using the in-house software QDng. In the diabatic picture, the two-level Hamiltonian reads as:

$$\hat{H} = \begin{pmatrix} \hat{V}_1 + \hat{T} & \hat{V}_{12} \\ \hat{V}_{12} & \hat{V}_2 + \hat{T} \end{pmatrix}, \quad (10)$$

where \hat{T} is the kinetic energy operator

$$\hat{T} = -\frac{\hbar^2}{2\mu} \sum_i \nabla_{q_i}^2 \quad (11)$$

while \hat{V}_1 and \hat{V}_2 are the potential energy operators, respectively for S_1 and S_2 , and \hat{V}_{12} is the diabatic coupling operator. The Arnoldi scheme [48–50] was employed as the propagator for all calculations. The reduced masses, μ , the time steps, Δt , and the number of grid points employed have been all summarized in table I. A Δt of 4 is equal to 96.75 as, while a reduced mass of 18000 is approximately 10 amu. For the initial state, assumed to be the result of a short-fs excitation pulse, the nuclear wave packet was approximated by a Gaussian envelope on S_2 . Lastly, a perfectly matched layer [51] was employed to absorb the wave packets at the boundary and to account for

the dissociative behaviour. The propagated wave pack-

	μ (au)	Δt (au)	Grid p.
C_i	18000	4	256x256
C_s	30000	2	300x300

Table I. Reduced masses, time steps and number of grid points used in the simulations.

ets were used for the evaluation of the expectation value of the polarizability, $\langle\hat{\alpha}\rangle$. Finally, the TRUECARs spectra were calculated with eq. (1) at different values of the pump-probe delay, T .

IV. RESULTS

For each system we have simulated two spectra with the conventional TRUECARs probe scheme, containing purely electronic or vibrational signals, as displayed in fig. 4. This was achieved by simulating the vibrational contribution ($\langle\phi_1|\alpha_{11}|\phi_1\rangle + \langle\phi_2|\alpha_{22}|\phi_2\rangle$) and the electronic contribution ($2\Re\langle\phi_1|\alpha_{12}|\phi_2\rangle$) separately. This distinction will help us break down the interesting characteristics of the spectra and highlight the differences and similarities between the probe schemes. It should be emphasized that the distinction of vibrational and electronic degrees of freedom near a conical intersection is fictitious, as these degrees of freedom are mixed.

Signals in fig. 4 have been normalized with respect to the maximum value of the vibrational contribution in the C_s model (panel (d)) with the following ratios: (a) $2 \cdot 10^{-4}$, (b) 0.78 and (c) 0.33. By comparing the overall intensities between the two models, we notice that the electronic contribution in the C_s is higher than the C_i system. The vibrational signals are, in both model systems, contained within the $0 \leq \omega_R \leq 1.5$ eV range and immediately visible in the spectrum due to vibrational coherences ($\langle\phi_2|\alpha_{22}|\phi_2\rangle$), whereas the electronic signals spread over a broader energy range ($0 \leq \omega_R \leq 2$ eV) and only appear after the wave packet has reached the CI. Hence, if the energy resolution is not sufficient, the two will overlap with each other and the electronic component may be masked by the stronger vibrational signal. A major difference between the two components can be seen in the temporal oscillations, where the electronic contribution to the signal oscillates much faster than the vibrational one.

In contrast to the conventional hybrid probe, here pulse trains have been employed instead of single Gaussian pulses. The following three combination schemes have been investigated:

- (I) An APT as ε_1 and a Gaussian pulse as ε_0^* ;
- (II) A Gaussian pulse as ε_1 and an APT as ε_0^* ;
- (III) Two identical APTs as both fields.

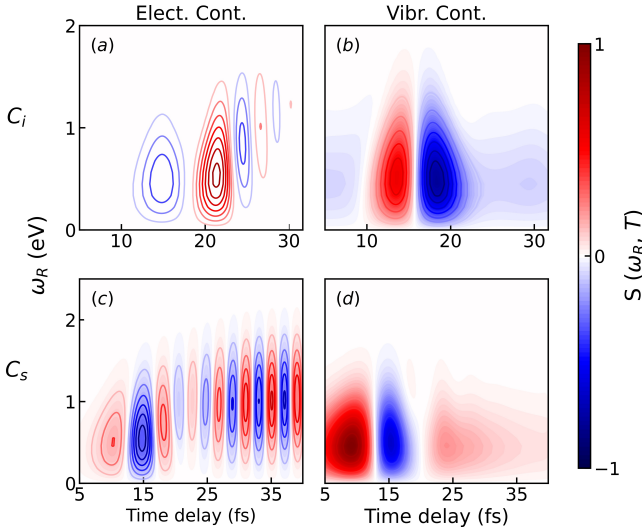


Figure 4. Comparison of electronic and vibrational contributions to the TRUECARs signals for Gaussian pulses. (a): electronic contribution in the C_i model; (b): vibrational contribution in the C_i model; (c): electronic contribution in the C_s model; (d): vibrational contribution in the C_s model. Spectra in the same row share the same Raman shift axis. The signals have been normalized with respect to the maximum value of (d).

In the following, we use σ_0 and σ_1 to indicate the Gaussian width of ε_0^* and ε_1 , respectively. Due to the nature of the pulse trains, multiple signals are expected in the spectra simulated with schemes (I) and (III). The extra signals arise from the side peaks of the train and are expected to be symmetric to each other, but they are lower in intensity with respect to the central signal at $\omega_R = 0$. In scheme (II), a Gaussian pulse in the femtosecond timescale is employed as ε_1 and the spectrum will mostly consist of one central signal. This is due to the limited spectral resolution of the femtosecond narrow band pulse. Spectra similar to fig. 4 but simulated with probe scheme (III), are given in the SI.

Calculations were carried out for different values of ω_{IR} at 1.55, 0.99 and 0.83 eV (i.e., $\lambda_{IR} = 800, 1250, 1500$ nm). The IR laser frequency is an important parameter in these calculations because it directly shapes the attosecond pulse train via the IR laser period, τ . A smaller τ implies more peaks in the time domain and, equivalently, less peaks in the frequency domain. Similarly, the σ_{env} parameter in eq. (5) can achieve the same effect.

A. C_s Symmetry Model

We begin our discussion of the results starting with the C_s model. The time evolution of the population of the excited states is plotted in the top panel of fig. 5. Following photoexcitation, the wave packet reaches the CI

in ≈ 12 fs with an overall population transfer of $\approx 45\%$. The electronic coherence reaches a maximum of 0.15 at 15 fs, after which starts decaying. The simulated APT TRUECARs spectra are shown in fig. 5 (c), (d) and (e) compared to a standard single pulse TRUECARs (b). The dashed black line in the spectra indicates the expectation value of the energy separation, $\Delta E_{21}(t)$, between S_1 and S_2 . For more details, see the S.I. of Ref. [40]. Because the spectrum is symmetric with respect to $\omega_R = 0$, only signals within $\omega_R \in [0, 2.5]$ eV are shown. Extra signals appear above 2.5 eV with schemes (I) and (III), however, those only carry redundant information, as they are lower-intensity replicas of the central peak. Initially, the vibrational coherence is the only contribution and it is constrained within $0 \leq \omega_R \leq 1.5$ eV, as shown in fig. 4. Once the wave packet is in the proximity of the CI, the electronic coherence starts to build up and becomes visible in the $0 \leq \omega_R \leq 2$ eV region of the spectrum. As the energy separation between the states increases again, the oscillating pattern of gain and loss features in the Stokes and anti-Stokes regime can be seen in the spectrum. The oscillation period directly mirrors the coherence period: as $\Delta E_{21}(t)$ grows, the oscillations speed up which causes the positions of the peaks in the Raman shift ω_R to spread apart. Due to the shape of the potential energy surfaces, the energy separation between S_2 and S_1 stays approximately constant after the CI. This can be seen from the dashed black lines in fig. 5 as well as the positions of the peaks in the Raman shift ω_R .

Among the three APT probe combinations displayed in fig. 5 only (c) is able to capture the CI signature at $\omega_{IR} = 1.55$ eV. By comparing panels 5(b) and (c), we note that scheme (I) can achieve similar energy resolution to the Gaussian/Gaussian hybrid probe, while being characterized by the presence of additional signals in the spectrum. However, probe scheme (I) still requires a single pulse in the attosecond time scale.

As the IR laser frequency decreases from 1.55 to 0.83 eV, the pulse train peaks get closer to each other in the spectral domain and the interesting electronic coherence fingerprint becomes visible in the spectra simulated with scheme (II), as displayed in fig. 6. This probe scheme does not require a single pulse in the attosecond regime. Moreover, it allows to achieve a better spectral resolution of the signals in the Raman shift than a standard TRUECARs (fig. 5(b)). In fact, the vibrational and electronic contributions are now sufficiently separated from each other to allow for an unambiguous assignment. The latter is not captured by the central harmonic of the APT but by its first side peak. This hypothesis was supported by simulations carried out varying the σ_{env} parameter, at the same ω_{IR} of fig. 6. The width of the Gaussian envelope directly shapes the width of the harmonics in the HHG spectrum. By increasing and decreasing the σ_{env} of the pulse train we noticed a corresponding increase and decrease in the separation between harmonics, and therefore between the vibrational and electronic contri-

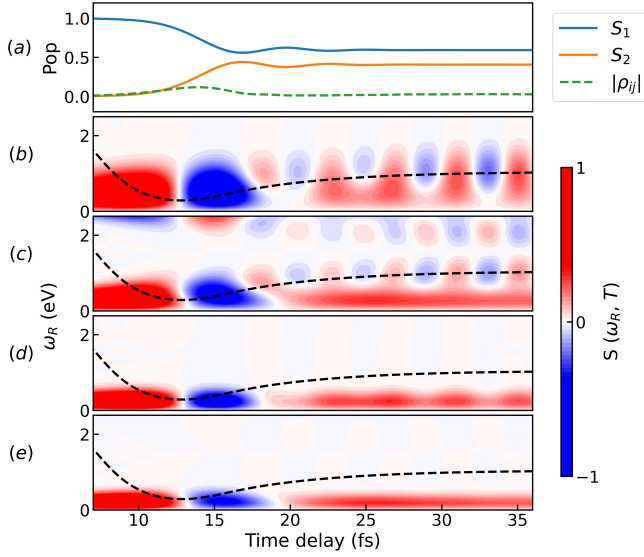


Figure 5. Comparison of pulse schemes for the C_s model system. (a): Time evolution of the population and the coherence of the two excited states in the diabatic basis. The population transfer is around 45% and occurs after about 15 fs of the wave packet propagation. The diabatic coupling is responsible for the slight oscillation in the population between 15 and 20 fs; (b) TRUECAR spectrum generated by an isolated Gaussian hybrid femtosecond/attosecond probe-pulse sequence (pulse parameters $\sigma_1 = 1.5$ and $\sigma_0 = 0.15$ fs). (c) TRUECAR spectrum obtained via combination (I) with Gaussian pulse parameter $\sigma_0 = 0.15$ fs; (d) TRUECAR spectrum obtained via combination (II) with Gaussian pulse parameter $\sigma_1 = 1.5$ fs; (e) TRUECAR spectrum obtained via combination of two identical APTs (scheme (III)). Each signal has been normalized with respect to its maximum value. The dashed black line represents the average time-dependent separation of the adiabatic potential energy surfaces. All spectra are simulated for $\omega_{IR} = 1.55$ eV. A snapshot of the pulse train can be found in fig. 2.

bution in the TRUECAR signal. The oscillation in fig. 6 appears to be slightly shifted in the Raman shift and does not follow the dashed black line anymore. Nevertheless, the oscillation period is the same and can still be used to obtain information on CI. According to the calculations, for this specific system an IR laser frequency of 0.83 eV appears to be the most suited to resolve the time-dependent energy gap between the two PESs, as shown in fig. 6(a).

We can extract additional insight from the oscillation period by analyzing the Wigner distribution [52–54] or temporal gating spectrogram of the analytic signal [55], which display a time-frequency map. The Wigner distribution is defined as

$$W(T, \omega) = \int_{-\infty}^{\infty} d\tau S_a\left(T + \frac{\tau}{2}\right) S_a^*\left(T - \frac{\tau}{2}\right) e^{i\omega\tau} \quad (12)$$

where $S_a(T)$ is the so-called analytic signal whose imaginary part is related to the original signal, $S(T)$, by

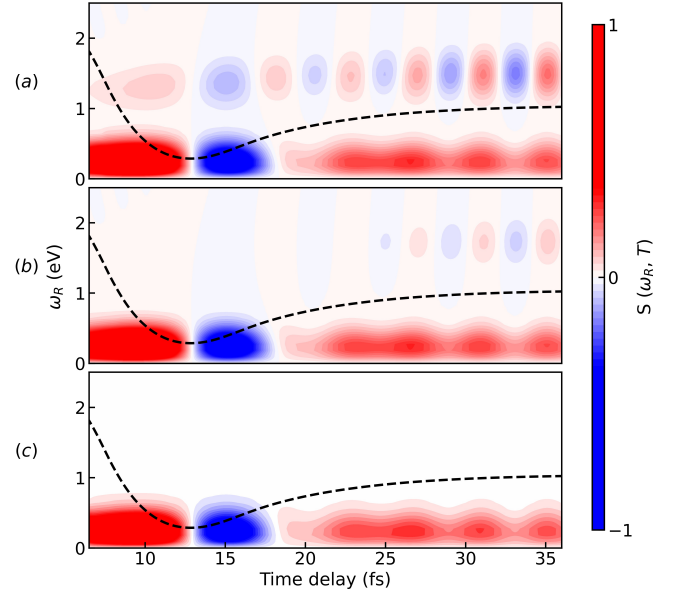


Figure 6. Simulated TRUECAR spectra for increasing values of the generating IR laser frequency with probe scheme (II), for the C_s system. (a): $\omega_{IR} = 0.83$ eV; (b): $\omega_{IR} = 0.99$ eV; (c): $\omega_{IR} = 1.55$ eV. The Gaussian pulse employed as ε_1 has a width of $\sigma_1 = 1.5$ fs. The dashed black line represents the average time-dependent separation of the adiabatic potential energy surfaces.

Hilbert transformation:

$$S_a(T) = S(T) + \frac{i}{\pi} \int_{-\infty}^{\infty} ds \frac{S(T-s)}{s} \quad (13)$$

Here, $S(T) \equiv S(T; \omega_R)$ is a temporal slice of the signal in fig. 6(a) at a selected Raman shift. The Wigner distribution is a quadratic functional of the signal and so it will, in general, show interference between the negative and positive frequency components of the signal. However, when the analytic signal is used in the computation, no negative frequencies are present, hence no interference will survive in the spectrogram. Figure 7(b) and (d) show the modulus $|W(T, \omega)|$ for signal traces taken at $\omega_R = 1.56$ and 0.27 eV, which are interpreted as electronic and vibrational contributions respectively. Panels 7(a) and (c) capture the different temporal oscillations of the vibrational and electronic components of the TRUECAR signal. The electronic Wigner distribution spans a broader frequency window than the vibrational contribution. Such window represents the PESs splitting in proximity of the CI. More strikingly, the energy splitting of the main electronic feature is time-dependent and starts around 0.25 eV at 10 fs and converges to 1 eV at ≈ 25 fs. This is in good agreement with the indicated splitting (black dashed line) in figs. 5 and 6.

With probe scheme (III) (fig. 5(e)) the characteristic features caused by electronic coherence are concealed in the spectrum. This happens because the small oscillation, traceable to the electronic component of the

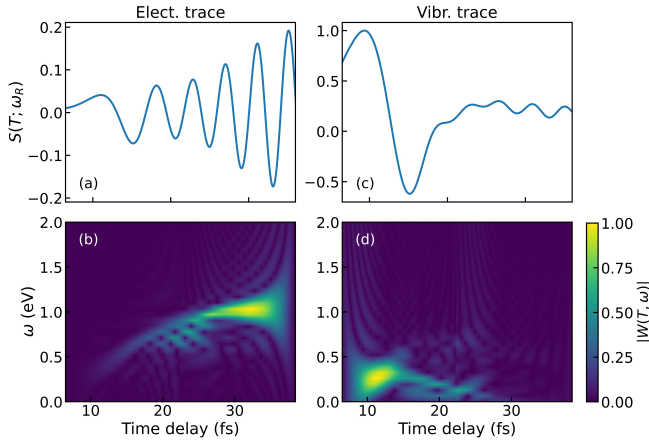


Figure 7. Comparison between Wigner distributions of selected traces of the TRUECARs signal. (a) and (c): Signal traces $S(T; \omega_R)$ at $\omega_R = 1.56$ and 0.27 eV, respectively. (b) and (d): Normalized Wigner spectrograms of (a) and (c). The frequency information obtained from the spectrogram is extracted from the temporal features of the signal.

TRUECARs signal, overlaps with the dominant vibrational contribution in the same region.

B. C_i Symmetry Model

The time evolution of the population of the two excited states, S_2 and S_1 , as well as the electronic coherence magnitude, is displayed in fig. 8(a) for the C_i model system. The wave packet takes about 15 fs to reach the conical intersection, resulting in an overall population transfer of $\sim 45\%$. The electronic coherence has a maximum of 0.0015 around 15 fs, after which starts decaying because of the increasing energy splitting between the surfaces.

Following the photoexcitation on S_2 , as the original wave packet approaches the CI, the wave packet transferred on S_1 will inherit an odd symmetry from the diabatic couplings. This generates a very weak electronic coherence (10^{-3} order of magnitude) because the integral $2\Re\langle\phi_1|\phi_2\rangle$ gets very small. Hence, the vibronic coherence, which TRUECARs is sensible to via the physical observable $\langle\hat{\alpha}\rangle$, has now a dominant vibrational component that totally conceal the interesting and characteristic features of the CI, such as the time-dependent energy splitting. This is why we are not able to observe them with the TRUECARs technique for this model system, not even with the standard single Gaussian pulse probe scheme of fig. 8(b). Decreasing the IR frequency from $\omega_{IR} = 1.55$ to 0.83 eV does not produce any significant change. The reason why this does not occur in the C_s model is due to the small shift of S_2 in q_2 , breaking the symmetry and making the integral larger.

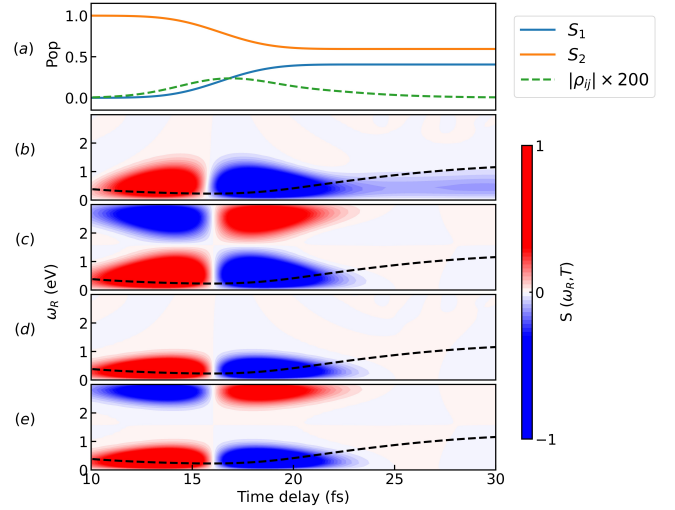


Figure 8. Comparison of pulse schemes for the C_i model system. (a): Time evolution of the populations and coherence for states S_1 and S_2 in the diabatic basis. The coherence magnitude (in green) has been magnified by a factor of 200 for visual purposes. The population transfer ($\sim 45\%$) occurs after about 15 fs when the wave packet reaches the CI. (b): TRUECARs spectrum generated by an isolated Gaussian hybrid femtosecond/attosecond probe-pulse sequence (pulse parameters $\sigma_1 = 1.5$ and $\sigma_0 = 0.15$ fs). (c): TRUECARs spectrum obtained via combination (I) with Gaussian pulse parameter $\sigma_0 = 0.15$ fs; (d): TRUECARs spectrum obtained via combination (II) with Gaussian pulse parameter $\sigma_1 = 1.5$ fs; (e): TRUECARs spectrum obtained via combination (III). The dashed black line represents the average time-dependent separation of the adiabatic potential energy surfaces. All are spectra are calculated at $\omega_{IR} = 1.55$ eV. Each signal has been normalized with respect to its maximum value. A snapshot of the pulse train is displayed in fig. 2.

V. CONCLUSIONS

In this paper, we tested the suitability of attosecond pulse trains as probes for detecting electronic coherence generated at a conical intersection with the TRUECARs technique. Model systems of different symmetry and two nuclear degrees of freedom were used. The polarizability matrices were modelled to obtain Raman active vibrational modes. The inclusion of the diagonal polarizability matrix elements includes vibrational coherences, which are inevitably a part of the signal. The full vibronic polarizability matrix must be taken into account in order to be basis-independent and the diagonal matrix elements cannot be neglected when transforming between adiabatic and diabatic representations. Although this leads to a more complex signal, we could show that it is still possible to distinguish the fast oscillating electronic feature from the vibrational contribution by analyzing the temporal gating spectrogram.

To gain additional insight into the TRUECARs signals, spectra originated from purely electronic or purely

vibrational contributions were simulated by evaluating the off-diagonal and diagonal contribution separately in the time-dependent expectation value of the polarizability operator. Due to symmetry and Raman selection rules, the electronic coherence appears to vanish in the C_i model system and concealed by the much stronger vibrational contributions.

We have explored three different schemes for the probe pulse and discussed their features in comparison to the conventional TRUECARS scheme. We found that, among the schemes reviewed, the combination of a Gaussian pulse as a narrowband pulse and an attosecond pulse train as the broad band pulse proved to be the most suitable for our purposes, offering two main advantages: first, a more clear separation between the electronic and vibrational components of the TRUECARS signal can be achieved by fine-tuning the IR laser frequency. The convolution of harmonics leads to a shift of the peaks in the spectral domain, but the energy separation can still be read off the oscillation period in the time domain. This was corroborated by the analysis of Wigner spectrograms, calculated for selected temporal traces of the signal. Second, single Gaussian pulses in the attosecond timescale are no longer required. Furthermore, this is the logical choice for the hybrid probe used in TRUECARS, since the Gaussian pulse and the APT represent a narrowband and a broad band pulse, respectively. The calculations showed the best results at $\omega_{IR} = 0.83$ eV.

The probe scheme with an APT and a Gaussian pulse, employed as narrowband pulse and broad band pulse respectively, also proved to be suitable to capture the CI fingerprints. Whereas the traditional TRUECARS spectrum is composed of one main signal centered at $\omega_R = 0$, multiple bands are now visible. Such bands are replicas of the main central signal with scaled intensities, and are visible along the harmonic comb where the side peaks of

the pulse train appear. When compared, the two spectra contain similar information about the detected vibronic coherence. Nevertheless, such combination for the probe still requires a single attosecond pulse acting as a broad-band pulse.

The use of two identical pulse trains did not reveal most features related to the electronic coherence in the simulated spectrum. Due to the insufficient resolution, the electronic component overlaps with the dominant vibrational signal, resulting in a concealment of the electronic contribution.

SUPPLEMENTARY MATERIAL

The supplementary material provides: *i*) snapshots of the modeled attosecond pulse train shape at selected frequencies of the generating IR laser; *ii*) details about modeling of the material properties as well as the potential energy surfaces and the diabatic couplings used for the C_i and C_s systems; *iii*) TRUECARS spectra displaying the entire frequency comb of the attosecond pulse train.

ACKNOWLEDGMENTS

This project has received funding from the European Union’s Horizon 2020 research and innovation program under the Marie Skłodowska-Curie grant agreement No. 860553 and the Swedish Research Council (Grant No. VR 2018-05346).

DATA AVAILABILITY

The data that support the findings of this study are available from the corresponding author upon reasonable request.

-
- [1] E. Teller. The crossing of potential surfaces. *J. Phys. Chem.*, 41(1):109–116, 1937.
 - [2] D. R. Yarkony. Conical intersections: Diabolical and often misunderstood. *Acc. Chem. Res.*, 31(8):511–518, 1998.
 - [3] G. A. Worth and L. S. Cederbaum. Beyond Born-Oppenheimer: molecular dynamics through a conical intersection. *Annu. Rev. Phys. Chem.*, 55:127–158, 2004.
 - [4] W. Domcke, D. R. Yarkony, and H. Köppel. *Conical intersections: theory, computation and experiment*, volume 17. World Scientific, 2011.
 - [5] V. Balzani, P. Piotrowiak, M. A. J. Rodgers, J. Mattay, D. Astruc, et al. *Electron transfer in chemistry*, volume 1. Wiley-VCH Weinheim, 2001.
 - [6] H. E. Zimmerman. Molecular orbital correlation diagrams, Mobius systems, and factors controlling ground- and excited-state reactions. ii. *J. Am. Chem. Soc.*, 88(7):1566–1567, 1966.
 - [7] M. Klessinger and J. Michl. *Excited states and photochemistry of organic molecules*. VCH publishers, 1995.
 - [8] M. Chergui. Ultrafast photophysics of transition metal complexes. *Acc. Chem. Res.*, 48(3):801–808, 2015.
 - [9] M. A. Robb, M. Garavelli, M. Olivucci, and F. Bernardi. A computational strategy for organic photochemistry. *Rev. Comput. Chem.*, 15:87–146, 2000.
 - [10] H.-G. Duan and M. Thorwart. Quantum mechanical wave packet dynamics at a conical intersection with strong vibrational dissipation. *J. Phys. Chem. Lett.*, 7(3):382–386, 2016.
 - [11] W. Domcke, D. Yarkony, and H. Köppel. *Conical intersections: electronic structure, dynamics & spectroscopy*, volume 15. World Scientific, 2004.
 - [12] W. Domcke and D. R. Yarkony. Role of conical intersections in molecular spectroscopy and photoinduced chemical dynamics. *Annu. Rev. Phys. Chem.*, 63:325–352, 2012.
 - [13] S. Rinaldi, F. Melaccio, S. Gozem, F. Fanelli, and M. Olivucci. Comparison of the isomerization mechanisms of human melanopsin and invertebrate rhodopsins. *Proc. Natl. Acad. Sci. U.S.A.*,

- 111(5):1714–1719, 2014.
- [14] D. Polli, P. Altoe, O. Weingart, K. M. Spillane, C. Manzoni, D. Brida, G. Tomasello, G. Orlandi, P. Kukura, R. A. Mathies, et al. Conical intersection dynamics of the primary photoisomerization event in vision. *Nature*, 467(7314):440–443, 2010.
- [15] L. S. Cederbaum, W. Domcke, H. Köppel, and W. Von Niessen. Strong vibronic coupling effects in ionization spectra: The “mystery band” of butatriene. *Chem. Phys.*, 26(2):169–177, 1977.
- [16] L. S. Cederbaum, H. Köppel, and W. Domcke. Multimode vibronic coupling effects in molecules. *Int. J. Quantum Chem.*, 20(S15):251–267, 1981.
- [17] L. Young, K. Ueda, M. Gühr, P. H. Bucksbaum, M. Simon, S. Mukamel, N. Rohringer, K. C. Prince, C. Masciovecchio, M. Meyer, et al. Roadmap of ultrafast X-ray atomic and molecular physics. *J. Phys. B*, 51(3):032003, 2018.
- [18] S. Rahav and S. Mukamel. Ultrafast nonlinear optical signals viewed from the molecules perspective: Kramers-Heisenberg transition amplitudes vs. susceptibilities. *Adv. At. Mol. Opt. Phys.*, 59:223, 2010.
- [19] T. Horio, T. Fuji, Y. Suzuki, and T. Suzuki. Probing ultrafast internal conversion through conical intersection via time-energy map of photoelectron angular anisotropy. *J. Am. Chem. Soc.*, 131(30):10392–10393, 2009.
- [20] T. A. A. Oliver, N. H. C. Lewis, and G. R. Fleming. Correlating the motion of electrons and nuclei with two-dimensional electronic-vibrational spectroscopy. *Proc. Natl. Acad. Sci. U.S.A.*, 111(28):10061–10066, 2014.
- [21] B. K. McFarland, J. P. Farrell, S. Miyabe, F. Taranelli, A. Aguilar, N. Berrah, C. Bostedt, J. D. Bozek, P. H. Bucksbaum, J. C. Castagna, et al. Ultrafast X-ray Auger probing of photoexcited molecular dynamics. *Nat. Commun.*, 5(1):1–7, 2014.
- [22] M. C. Galbraith, S. Scheit, N. V. Golubev, G. Reitsma, N. Zhavoronkov, V. Despré, F. Lepine, A. I. Kuleff, M. J. J. Vrakking, O. Kornilov, et al. Few-femtosecond passage of conical intersections in the benzene cation. *Nat. Commun.*, 8(1):1–7, 2017.
- [23] K. Sun, W. Xie, L. Chen, W. Domcke, and M. F. Gelin. Multi-faceted spectroscopic mapping of ultrafast nonadiabatic dynamics near conical intersections: A computational study. *J. Chem. Phys.*, 153(17):174111, 2020.
- [24] J. Yang, X. Zhu, T. J. A. Wolf, Z. Li, J. P. F. Nunes, R. Coffee, J. P. Cryan, M. Gühr, K. Hegazy, T. F. Heinz, et al. Imaging CF₃I conical intersection and photodissociation dynamics with ultrafast electron diffraction. *Science*, 361(6397):64–67, 2018.
- [25] T. J. A. Wolf, R. H. Myhre, J. P. Cryan, S. Coriani, R. J. Squibb, A. Battistoni, N. Berrah, C. Bostedt, P. Bucksbaum, G. Coslovich, et al. Probing ultrafast $\pi\pi^*/n\pi^*$ internal conversion in organic chromophores via K-edge resonant absorption. *Nat. Commun.*, 8(1):1–7, 2017.
- [26] K. F. Chang, M. Reduzzi, H. Wang, S. M. Poullain, Y. Kobayashi, L. Barreau, D. Prendergast, D. M. Neumark, and S. R. Leone. Revealing electronic state-switching at conical intersections in alkyl iodides by ultrafast XUV transient absorption spectroscopy. *Nat. Commun.*, 11(1):1–7, 2020.
- [27] K. S. Zinchenko, F. Ardana-Lamas, I. Seidu, S. P. Neville, J. van der Veen, V. U. Lanfalon, M. S. Schurman, and H. J. Wörner. Sub-7-femtosecond conical-intersection dynamics probed at the carbon K-edge. *Science*, 371(6528):489–494, 2021.
- [28] Y. Nam, D. Keefer, A. R. Nenov, I. Conti, F. Aleotti, F. Segatta, J. Y. Lee, M. Garavelli, and S. Mukamel. Conical intersection passages of molecules probed by X-ray diffraction and stimulated Raman spectroscopy. *J. Phys. Chem. Lett.*, 12:12300–12309, 2021.
- [29] S. P. Neville, M. Chergui, A. Stolow, and M. S. Schurman. Ultrafast X-ray spectroscopy of conical intersections. *Phys. Rev. Lett.*, 120(24):243001, 2018.
- [30] N. Rohringer. X-ray Raman scattering: a building block for nonlinear spectroscopy. *Philos. Trans. R. Soc. A*, 377(2145):20170471, 2019.
- [31] M. Ferray, A. L’Huillier, X. F. Li, L. A. Lompre, G. Mainfray, and C. Manus. Multiple-harmonic conversion of 1064 nm radiation in rare gases. *J. Phys. B*, 21(3):L31, 1988.
- [32] K. Varju, P. Johnsson, J. Mauritsson, A. L’Huillier, and R. Lopez-Martens. Physics of attosecond pulses produced via high harmonic generation. *Am. J. Phys.*, 77(5):389–395, 2009.
- [33] C. Pellegrini, A. Marinelli, and S. Reiche. The physics of X-ray free-electron lasers. *Rev. Mod. Phys.*, 88(1):015006, 2016.
- [34] G. Farkas and C. Tóth. Proposal for attosecond light pulse generation using laser induced multiple-harmonic conversion processes in rare gases. *Phys. Lett. A*, 168(5-6):447–450, 1992.
- [35] S. E. Harris, J. J. Macklin, and T. W. Hänsch. Atomic scale temporal structure inherent to high-order harmonic generation. *Opt. Commun.*, 100(5-6):487–490, 1993.
- [36] M. Hentschel, R. Kienberger, C. Spielmann, G. A. Reider, N. Milosevic, T. Brabec, P. Corkum, U. Heinzmann, M. Drescher, and F. Krausz. Attosecond metrology. *Nature*, 414(6863):509–513, 2001.
- [37] P. Paul, E. S. Toma, P. Breger, G. Mullot, F. Augé, P. Balcou, H. G. Muller, and P. Agostini. Observation of a train of attosecond pulses from high harmonic generation. *Science*, 292(5522):1689–1692, 2001.
- [38] D. Jadoun and M. Kowalewski. Time-resolved photoelectron spectroscopy of conical intersections with attosecond pulse trains. *J. Phys. Chem. Lett.*, 12:8103–8108, 2021.
- [39] A. Marciniak, V. Despré, V. Lorient, G. Karras, M. Hervé, L. Quintard, F. Catoire, C. Joblin, E. Constant, A. I. Kuleff, and F. Lépine. Electron correlation driven non-adiabatic relaxation in molecules excited by an ultrashort extreme ultraviolet pulse. *Nature Commun.*, 10(1):337, 2019.
- [40] M. Kowalewski, K. Bennett, K. E. Dorfman, and S. Mukamel. Catching conical intersections in the act: Monitoring transient electronic coherences by attosecond stimulated X-ray Raman signals. *Phys. Rev. Lett.*, 115:193003, 2015.
- [41] M. Kowalewski, B. P. Fingerhut, K. E. Dorfman, K. Bennett, and S. Mukamel. Simulating coherent multidimensional spectroscopy of nonadiabatic molecular processes: From the infrared to the X-ray regime. *Chem. Rev.*, 117(19):12165–12226, 2017.
- [42] H. C. Longuet-Higgins. The symmetry groups of non-rigid molecules. *Mol. Phys.*, 6(5):445–460, 1963.
- [43] R. Obaid and M. Leibscher. A molecular symmetry analysis of the electronic states and transition dipole moments for molecules with two torsional degrees of freedom. *J. Chem. Phys.*, 142(6):064315, 2015.

- [44] I. J. Palmer, I. N. Ragazos, F. Bernardi, M. Olivucci, and M. A. Robb. An MC-SCF study of the S1 and S2 photochemical reactions of benzene. *J. Am. Chem. Soc.*, 115(2):673–682, 1993.
- [45] H. Köppel, B. Schubert, and H. Lischka. Conical intersections and strong nonadiabatic coupling effects in singlet-excited acetylene: An ab initio quantum dynamical study. *Chem. Phys.*, 343(2):319–328, 2008.
- [46] D. R. Yarkony. Diabolical conical intersections. *Rev. Mod. Phys.*, 68:985–1013, Oct 1996.
- [47] D. J. Tannor. *Introduction to quantum mechanics: a time-dependent perspective*. 2007.
- [48] W. E. Arnoldi. The principle of minimized iterations in the solution of the matrix eigenvalue problem. *Q. Appl. Math.*, 9(1):17–29, 1951.
- [49] R. A. Friesner, L. S. Tuckerman, B. C. Dornblaser, and T. V. Russo. A method for exponential propagation of large systems of stiff nonlinear differential equations. *J. Sci. Comput.*, 4(4):327–354, 1989.
- [50] Y. Saad. Variations on Arnoldi’s method for computing eigenelements of large unsymmetric matrices. *Linear Algebra Appl.*, 34:269–295, 1980.
- [51] A. Nissen, H. O. Karlsson, and G. Kreiss. A perfectly matched layer applied to a reactive scattering problem. *J. Chem. Phys.*, 133(5):054306, 2010.
- [52] D. Keefer, T. Schnappinger, and S. de Vivie-Riedle, R. and Mukamel. Visualizing conical intersection passages via vibronic coherence maps generated by stimulated ultrafast X-ray Raman signals. *Proc. Natl. Acad. Sci. U.S.A.*, 117(39):24069–24075, 2020.
- [53] S. M. Cavaletto, D. Keefer, and S. Mukamel. High temporal and spectral resolution of stimulated X-ray Raman signals with stochastic free-electron-laser pulses. *Phys. Rev. X*, 11(1):011029, 2021.
- [54] S. M. Cavaletto, D. Keefer, J. R. Rouxel, F. Aleotti, F. Segatta, M. Garavelli, and S. Mukamel. Unveiling the spatial distribution of molecular coherences at conical intersections by covariance x-ray diffraction signals. *Proc. Natl. Acad. Sci. U.S.A.*, 118(22), 2021.
- [55] B. Boashash. Note on the use of the wigner distribution for time-frequency signal analysis. *IEEE Trans. Signal Process.*, 36(9):1518–1521, 1988.